Available online at www.sciencedirect.com
ScienceDirect
Journal of Computational Physics 220 (2007) 586–611
JOURNAL OF COMPUTATIONAL PHYSICS
www.elsevier.com/locate/jcp

The numerical prediction of planar viscoelastic contraction flows using the pom–pom model and higher-order finite volume schemes

J.P. Aguayo [a], P.M. Phillips [b], T.N. Phillips [c,*], H.R. Tamaddon-Jahromi [a], B.A. Snigerev [b], M.F. Webster [a]

[a] *Department of Computer Science, University of Wales, Swansea SA2 8PP, United Kingdom*
[b] *Department of Mathematics, University of Wales, Aberystwyth SY23 3BZ, United Kingdom*
[c] *School of Mathematics, Cardiff University, Senghennydd Road, Cardiff CF24 4AG, United Kingdom*

Received 20 December 2005; received in revised form 19 May 2006; accepted 19 May 2006
Available online 17 July 2006

Abstract

This study investigates the numerical solution of viscoelastic flows using two contrasting high-order finite volume schemes. We extend our earlier work for Poiseuille flow in a planar channel and the single equation form of the extended pom–pom (SXPP) model [M. Aboubacar, J.P. Aguayo, P.M. Phillips, T.N. Phillips, H.R. Tamaddon-Jahromi, B.A. Snigerev, M.F. Webster, Modelling pom–pom type models with high-order finite volume schemes, J. Non-Newtonian Fluid Mech. 126 (2005) 207–220], to determine steady-state solutions for planar 4:1 sharp contraction flows. The numerical techniques employed are time-stepping algorithms: one of hybrid finite element/volume type, the other of pure finite volume form. The pure finite volume scheme is a staggered-grid cell-centred scheme based on area-weighting and a semi-Lagrangian formulation. This may be implemented on structured or unstructured rectangular grids, utilising backtracking along the solution characteristics in time. For the hybrid scheme, we solve the momentum-continuity equations by a fractional-staged Taylor–Galerkin pressure-correction procedure and invoke a cell-vertex finite volume scheme for the constitutive law. A comparison of the two finite volume approaches is presented, concentrating upon the new features posed by the pom–pom class of models in this context of non-smooth flows. Here, the dominant feature of larger shear and extension in the entry zone influences both stress and stretch, so that larger stretch develops around the re-entrant corner zone as Weissenberg number increases, whilst correspondingly stress levels decline.

Keywords: Pom–pom model; Pure finite volume; Hybrid finite element/volume; Abrupt contraction; Viscoelasticity

* Corresponding author. Tel.: +44 2920 874194; fax: +44 2920 874199.
E-mail addresses: csjuan@swan.ac.uk (J.P. Aguayo), pmp97@aber.ac.uk (P.M. Phillips), PhillipsTN@cf.ac.uk (T.N. Phillips), cshamid@swan.ac.uk (H.R. Tamaddon-Jahromi), snigerev@mail.knc.ru (B.A. Snigerev), M.F.Webster@swan.ac.uk (M.F. Webster).

0021-9991/$ - see front matter
doi:10.1016/j.jcp.2006.05.039

1. Introduction

This paper is concerned with the prediction of the flow of branched polymer melts through a 4:1 planar contraction using the extended pom–pom (XPP) model of Verbeeten et al. [36]. There have been a number of extensions to the tube kinetic model for entangled melts developed by Doi and Edwards [16], including the Double Convected Reptation (DCR) model of Ianniruberto and Marrucci [24], the pom–pom model of McLeish and Larson [25], as well as versions of the extended pom–pom model [36]. These models possess two features that are absent from phenomenological models such as the Oldroyd-B model. The first feature recognises the dependency of melt rheology on the molecular structure of the polymer, whilst the second recognises that the spectrum of relaxation times leads to partial differential equations for the orientation and stretch.

The original pom–pom model of McLeish and Larson [25] is based on an idealised polymer molecule in which the polymer chains are represented by a backbone segment connecting two identical pom–poms each with q arms at the branch points. The drag that the melt exerts on these arms causes the backbone to stretch. The branch points slow down the reptation motion of the backbone by pinning the molecule in place at the tube junctions. The free ends of the arms are still able to move, however, and the polymer is able to free itself from the tube by a process known as arm-retraction, which is triggered when the molecule reaches its maximum stretched state. The arms gradually work their way out of the tubes towards the branch points by diffusion. Once the arms have relaxed, the backbone can subsequently relax by moving the branch points. The finite extensibility constraint on the backbone stretch gives rise to discontinuity in the gradient of the steady-state extensional viscosity.

Blackwell et al. [10] modified the evolution equation for the stretch to allow for branch point displacement. This had the effect of removing the discontinuity in steady-state extensional viscosity gradient. The two remaining major drawbacks in the original pom–pom model, viz. the prediction of a zero second normal stress-difference and the unboundedness of the backbone orientation equation, were addressed in the extended pom–pom (XPP) model developed by Verbeeten et al. [36].

In this paper numerical solutions are generated using two contrasting finite volume schemes: a hybrid cell-vertex scheme (FE/FV) and a pure cell-centred (SLFV) scheme. The schemes are described in the papers of Aboubacar and Webster [5] and Phillips and Williams [29], respectively. They are used to generate steady-state profiles for velocity, stretch and extra-stress in plane Poiseuille flow in [1]. These steady-state profiles are used as inflow conditions in the present work.

The planar 4:1 contraction problem has been at the forefront of computational rheology since it was adopted as a benchmark problem at the 5th international workshop on numerical methods in non-Newtonian flows [20]. It is now appreciated that the choice of 4:1 contraction ratio is limiting with respect to stimulation of a rich variety of interesting flow phenomena. An important exception to the lure of the 4:1 configuration is the recent paper of Alves et al. [7] who investigated the effect of varying contraction ratio on creeping flow characteristics in a planar contraction for a linear Phan-Thien/Tanner (PTT) fluid ($\epsilon = 0.25$), capable of moderate strain-hardening. Nevertheless, due to the extensive literature on the 4:1 contraction problem it remains an important benchmark problem on which to test the accuracy and stability of numerical schemes. A comprehensive account of experimental observations [17,18] and numerical predictions is given in the research monograph of Owens and Phillips [27] and the review paper of Walters and Webster [39]. We close with some introductory remarks, reporting on some of the contributions that have been made to the understanding of this subject.

Boger [11] and Evans and Walters [17,18] have shown that, under the assumption of creeping flow, different types of vortices are formed upstream of the contraction plane. The vortices tend to increase with elasticity for shear-thinning fluids. The numerical simulations of Alves et al. [7] agree with the visualisations of Evans and Walters [17] for the 1% aqueous solution of polyacrylamide in that a lip-vortex is neither predicted nor observed. Purnode and Crochet [32] attempted to predict the experimental results of Evans and Walters [17,18] using a single-mode Peterlin modification of the finite extension nonlinear elasticity (FENE-P) model. There, model parameters were chosen to match the steady shear and extensional properties of each of the different concentrations of polyacrylamide (PAA) solutions with mild strain hardening at L^2-levels of 4–6. Although the essential vortex features of the experimental investigation, in salient-corner and around the

lip, were predicted in a qualitative sense over the range of contraction ratios and fluid concentrations, they did not concur at the same flow rates. This lack of quantitative agreement may be explained by appealing to the three-dimensional aspects involved in the experimental work and the inadequacy of the FENE-P model to capture all of the essential physics necessary for a complete description of these PAA solutions.

The numerical tools used by Purnode and Crochet [32] were based on a coupled finite element scheme developed by Marchal and Crochet [22,23]. In their first paper [22], Hermitian elements were introduced and found to enhance the limit of convergence in De[1] over the more conventional Lagrangian elements. In the Hermitian element approach, a continuous representation for the velocity gradient is considered. In their subsequent article [23], steady solutions were obtained for a wider range of values of Deborah number, De, with inconsistent streamline-upwinding (SU) and 4×4 linear stress subelements. A lip-vortex appeared at $De = 7.6$ when SU was used but disappeared by the time De had increased to 14. The authors speculated that this observation was a numerical artifact. The size and intensity of the salient corner vortex remained weak and insensitive to increasing elasticity. It should be noted, however, that the use of SU effectively alters the constitutive model and is therefore an inconsistent upwinding strategy.

Lip-vortices have also been observed by Yoo and Na [44] using a finite volume scheme based on the staggered grid SIMPLER methodology for an Oldroyd-B model. With an increase in De, the lip-vortex increased in size and intensity whilst the salient-corner vortex remained largely unchanged. Incorporating inertia had the effect of reducing the size and strength of the vortices, though lip-vortices still persisted. At low elasticity levels, the lip-vortex was distinct from the salient-corner vortex whilst, at higher elasticity levels, the lip and salient-corner vortices co-existed within a single recirculation cell.

Carew et al. [12] selected both Oldroyd-B and linear-PTT models (LPTT) for their numerical simulations with inertia included ($Re = 1$). For $\epsilon = 0.02$ and the LPTT model, a lip-vortex appeared at $We = 5$, which encapsulated the salient corner vortex upon increase of Weissenberg number up to $We = 10$, becoming the single established vortex at $We = 15$. In contrast, in the absence of inertia, no lip-vortex was present at $We = 5$. Also, for LPTT ($\epsilon = 0.25$) and $We = 10$, no evidence of lip-vortex activity was reported. The rheological departure here is the considerable reduction in levels of strain-hardening. Both LPTT-versions show no signs of strain-softening.

Recent work on finite volume discretisations substantiate these finite element findings. Phillips and Williams [31] reported lip-vortex activity for the flow of an Oldroyd-B fluid through a 4:1 planar contraction for $We > 2$. Alves et al. [8] reached identical conclusions for the UCM fluid in the same geometry, as did Aboubacar and Webster [5] and Xue et al. [43] for an Oldroyd-B fluid with $We > 1$. Substantial mesh refinement has been undertaken in these studies, yielding an accurate and reliable representation of vortex structure. Numerical investigations of Phillips and Williams [31] and Aboubacar and Webster [5] on the Oldroyd-B model with $\beta = 1/9$ have shown that a lip-vortex appears in the vicinity of $We = 2$. On coarser meshes, Aboubacar and Webster [5] predicted a lip-vortex for values of the Weissenberg number less than two, yet this feature disappeared with mesh refinement.

Bishko et al. [9] calculated the transient flow of a highly branched polymer melt in a planar 4:1 contraction using the differential approximation to the original pom–pom model. The governing equations were discretised using a Lagrangian finite element method. The size of the salient-corner vortex was found to increase with the degree of branching (q). This was attributed to the increased resistance to extension with branching. The polymers were largely undeformed within the vortex since the flow was weak in this region. The size of the vortex also increased with increasing Weissenberg number.

Tanner and Nasseri [34] analysed the response of shear and extensional viscosity of different constitutive models. There, a new form of single-mode PTT model, named PTT-XPP, was shown to be basically similar to the XPP model of Verbeeten et al. [36,37] in steady extension. However, this PTT-XPP model was noted to vary from the XPP model in shear viscosity at larger shear-rates. Clemeur et al. [15] investigated the performance of the double convected pom–pom model (DCPP), comparing simulation results for the abrupt con-

[1] The Deborah number (De) is defined by $De = \lambda_1\dot{\gamma}_w$, where $\dot{\gamma}_w$ is the fully-developed downstream wall shear rate and λ_1 is a relaxation time.

traction flow with experimental data. They found a deviation of 10–15% between experimental results and numerical predictions.

More recently, Verbeeten et al. [38] have simulated the transient flow of a low density polyethylene melt in a planar 3.29:1 contraction using multi-mode XPP models. The basis of the discretisation used is the finite element method with a Discrete Elastic-Viscous Split Stress/Discontinous Galerkin (DEVSS/DG) formulation. Convergence problems were encountered using the original XPP model with the DEVSS/DG method becoming unstable at higher levels of elasticity. However, convergence was achieved using a modified version of the XPP model in which the stretch dynamics were adjusted to be consistent with other viscoelastic models. This was in agreement with a modification proposed by Van Meerveld [26] based on non-equilibrium thermodynamics (see below for discussion). Quantitative comparisons with experimental data on velocity and stress profiles were presented. Good agreement was achieved except that the experimental stress along the centreline was underpredicted by this modified XPP model. A steady-state solution for a three-dimensional contraction geometry has also been reported by Sirakov et al. [33], using a multi-mode pom–pom model, comparing results against experimental data. They found that numerical predictions on vortex enhancement agreed with experimental evidence to within 15%. In contrast to the above, the present study is concerned with assessing the performance of two high-order finite volume schemes, where the novelty lies in extension of these methods to non-smooth flows (4:1 abrupt planar contraction) and single pom–pom models (SXPP).

2. Governing equations

The governing equations comprise the conservation equations for momentum and mass, together with a rheological equation of state. Here, we adopt the single equation version of the extended pom–pom (SXPP) model. This has been shown to be mathematically equivalent to the double equation formulation, involving a constitutive equation for the orientation tensor and an evolution equation for the stretch.

The governing equations are non-dimensionalised using scales on length (L, die-exit half-width), velocity (U, die-exit average-velocity), time (L/U), and pressure and extra-stress ($\mu U/L$). Here, $\mu = \mu_s + \mu_p$ is the total viscosity, with partial polymeric viscosity μ_p. To preserve similarity between the various constitutive law forms of the non-dimensional Oldroyd-B and SXPP models, we define $\mu_p = G_0\lambda_{0b}$. Dimensionless group numbers and parameters Re, We, β and ϵ, are defined by

$$Re = \frac{\rho UL}{\mu}, \quad We = \frac{\lambda_{0b}U}{L}, \quad \beta = \frac{\mu_s}{\mu_s + G_0\lambda_{0b}}, \quad \epsilon = \frac{\lambda_{0s}}{\lambda_{0b}}.$$

In this notational form, λ_{0b} and λ_{0s} represent the orientation and backbone stretch relaxation time-scales, respectively, and G_0 is the linear relaxation modulus. The parameter ϵ, the ratio of stretch to orientation relaxation times, is inversely proportional to the entanglement molecular weight of the backbone segments. Values of ϵ approaching unity correspond to molecules with relatively short backbone lengths, yet displaying long arms to retard the dynamics. Small values of ϵ correspond to highly entangled backbone configurations.

The equations of motion and continuity are represented viz,

$$\nabla \cdot \mathbf{u} = 0, \tag{1}$$

$$Re\left(\frac{\partial \mathbf{u}}{\partial t} + \mathbf{u}\cdot\nabla\mathbf{u}\right) = -\nabla p + \nabla\cdot(\boldsymbol{\tau} + 2\beta\mathbf{d}), \tag{2}$$

$$f(\lambda,\boldsymbol{\tau})\boldsymbol{\tau} + We\overset{\nabla}{\boldsymbol{\tau}} + \frac{(1-\beta)}{We}[f(\lambda,\boldsymbol{\tau})-1]\mathbf{I} + \frac{\alpha We}{(1-\beta)}\boldsymbol{\tau}\cdot\boldsymbol{\tau} = 2(1-\beta)\mathbf{d}, \tag{3}$$

with identity tensor $\mathbf{I}$. Here, $\overset{\nabla}{\boldsymbol{\tau}}$ and $f(\lambda,\boldsymbol{\tau})$ are given by

$$\overset{\nabla}{\boldsymbol{\tau}} = \frac{\partial\boldsymbol{\tau}}{\partial t} + \mathbf{u}\cdot\nabla\boldsymbol{\tau} - (\nabla\mathbf{u})^{\dagger}\cdot\boldsymbol{\tau} - \boldsymbol{\tau}\cdot(\nabla\mathbf{u}), \tag{4}$$

$$f(\lambda,\boldsymbol{\tau}) = \frac{2}{\epsilon}\left(1-\frac{1}{\lambda}\right)e^{\nu(\lambda-1)} + \frac{1}{\lambda^2}\left[1 - \left\{\frac{We}{(1-\beta)}\right\}^2\frac{\alpha}{3}I_{\boldsymbol{\tau}\cdot\boldsymbol{\tau}}\right], \tag{5}$$

with trace operator I and

$$\lambda = \sqrt{1 + \frac{We}{(1-\beta)}\frac{1}{3}|I_\tau|}. \tag{6}$$

Note, in (6) a negative backbone stretch (λ) is avoided by taking the absolute value of trace of the extra-stress (I_τ), Verbeeten et al. [37]. The parameter v in (5) was incorporated into the model by Blackwell et al. [10] to remove the discontinuity in the derivative of the extensional viscosity, present in the differential approximation of the original pom–pom model. Its value is estimated by data-fitting and found to be inversely proportional to the number of arms (q). More precisely, we have

$$v = \frac{2}{q}.$$

Finally, the total extra-stress can be written as the sum of polymeric ($\boldsymbol{\tau}$) and solvent contributions ($2\beta\mathbf{d}$).

In particular, the Oldroyd-B model corresponds to setting $\alpha = 0$ (isotropic) and $f(\lambda, \boldsymbol{\tau}) = 1$ in (3). If, in addition, $\beta = 0$, the UCM model is recovered. The constitutive equation (3) incorporates features of the Giesekus model, since for $\alpha \neq 0$ the model predicts a non-zero second normal stress-difference.

Through the current body of work, we have become of aware of further modifications to the pom–pom model (see [26,38]). The mathematical nature of these adjustments is to alter the multiplicative factor on the exponential term of Eq. (5) from $(1 - 1/\lambda)$ to $(1 - 1/\lambda^2)$. This has some impact on the extensional rheology for the material parameters chosen, over the decade of extension rates [1,10]; initially increasing strain-softening, then reversing this behaviour, before returning to similar softening response for $q = 2$. Equivalently, Trouton ratios are lessened. To get some feel for the relative significant of these model modifications, we can comment that typically at a moderate level of $We = 5$ ($q = 2, Re = 0$), stress and backbone stretch can be reduced in peak corner values by as much as O(10%). One might anticipate in accordance with Verbeeten et al. [38], that this may lead to enhanced levels of We_{crit} steady-state solutions. We note that by introducing $\alpha \neq 0$ to gain some influence from second normal stress-difference ($N_2 \neq 0$), we may also introduce the prospect of analytical singularities for some ranges of α-parameter even in homogenous flows [14]. This would become particularly prevalent at larger values of q. Singularity in the shear viscosity and first normal stress-coefficient was observed for $q = 15$ and $\alpha = 0.5$ in a 4:1 planar rounded-corner contraction (see [6]). Also, a flattening effect was noticeable in the extensional viscosity. The suggested modification to the model does not ease this situation in any way. These are issues we have investigated in some detail in [6].

Here, we describe the rheological properties of the extended pom–pom model in planar extensional and simple shear flow. Fig. 1 illustrates the steady-state shear and extensional viscosities, the Trouton ratio (T_r) and the backbone stretch. Viscosities are non-dimensionalised with respect to the zero shear-rate viscosity. By convention, the Trouton ratio is then normalised via a factor of 4. Shear and extensional rates are non-dimensionalised via the orientation relaxation time, λ_{0b}, and the rheological functions are plotted as functions of $\lambda_{0b}\dot{\gamma}$ or $\lambda_{0b}\dot{\epsilon}$, as appropriate. The steady-state viscosities of Fig. 1 are derived with the selected parameter values of $\epsilon = 1/3$, $q = 2$, $\alpha = 0.15$ and for $\beta = 1/9$.

The dimensionless steady-state shear viscosity of the XPP model exhibits a plateau at low shear-rates up to a dimensionless shear rate of around 0.2 followed by a shear-thinning regime in the shear-rate range $[1, 100]$. At higher shear-rates, the shear viscosity asymptotes to its second plateau, which approaches the value of β. The XPP model predicts strain-softening around $\lambda_{0b}\dot{\epsilon} \sim \mathrm{O}(2)$, a phenomenon apparently independent of β. At large dimensionless extension rates ($\lambda_{0b}\dot{\epsilon} > 10^4$) a second plateau regime develops in the extensional viscosity with limiting value of 4β. The corresponding Trouton ratio shows a peak around deformation rates O(10) before decaying away at larger values. In addition, the backbone stretch (λ) increases significantly and monotonically, when deformation-rates exceed 0.5 units (Fig. 1d). Such increase is present in both shear and extension, but more prominent in the latter and over the early deformation-rate range up to $\mathrm{O}(10^2)$. With respect to dependence on alternative parameter specification, the SXPP model can exhibit different levels of extension hardening that can be enhanced by increasing (q), and to a lesser degree via ϵ (also true for T_r). However, shear viscosity does not strongly depend on q and ϵ. Additionally, first normal stress coefficient (Ψ_1) shows weak dependence on q and ϵ, barring very high shear rates, when visible increment in (Ψ_1) can be observed upon

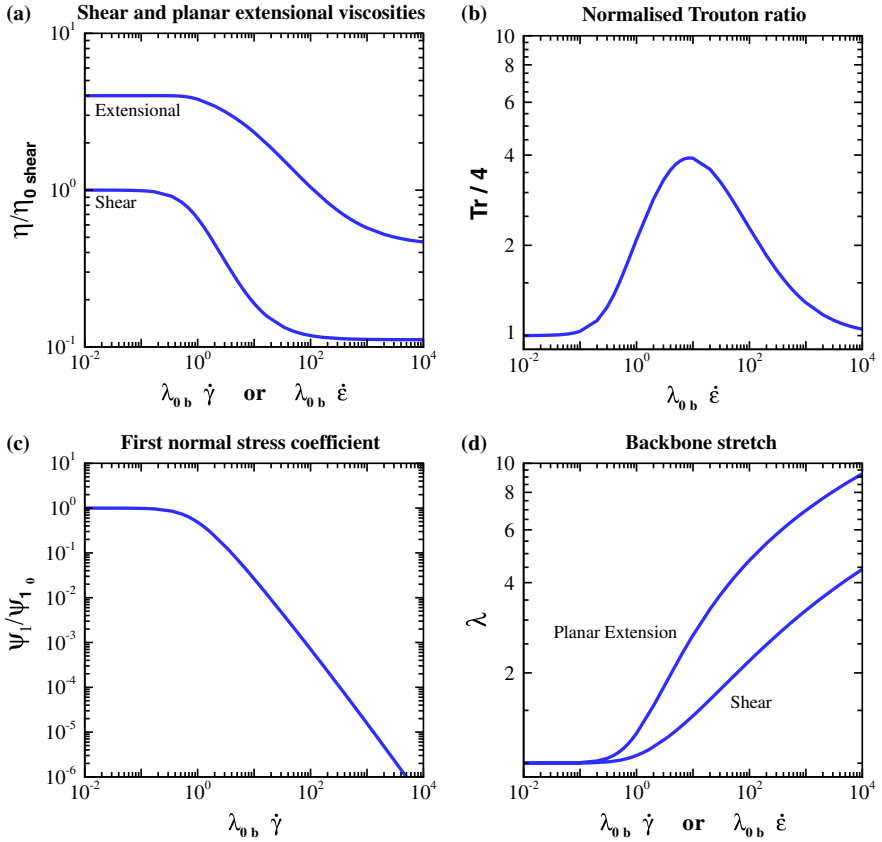

Fig. 1. Rheological properties of XPP model, $\beta = 1/9$, $\epsilon = 1/3$, $q = 2$ and $\alpha = 0.15$.

increasing q. Solvent/total viscosity ratio (β) affects plateau values in extensional (η_e) and shear (η_s) viscosity. When $\beta = 0$, there is no second plateau present in η_e, η_s or T_r. It is on this basis that our present selection of parameters has been taken, providing suitable material strain-softening properties to study, consistent with earlier background work.

3. Numerical schemes

Two contrasting finite volume schemes are studied, a hybrid cell-vertex scheme (FE/FV) and a pure cell-centred (SLFV) scheme. Both finite volume schemes employ a time-splitting construction to evolve the solution through time towards steady-state. In the case of the hybrid scheme, a semi-implicit formulation is employed in the momentum equation, based on a fractional-staged Taylor–Galerkin approach, with a pressure-correction step to enforce incompressibility. The pressure-correction (PC) aspects have been improved more recently to arrive at an incremental-PC implementation with enhanced temporal characteristics [19]. The hybrid cell-vertex scheme is based on a finite element discretisation of the conservation equations of mass and momentum and a finite volume discretisation of the constitutive equation. The finite volume grid is formed by partitioning each triangular finite element into four triangular cells by connecting the mid-side nodes of the element. This provides a stable approximation for viscoelastic flow problems and is close in philosophy to the so-called 4×4 stress subelement introduced by Marchal and Crochet [23]. Fluctuation distribution schemes (FD) are used to distribute the flux and source residuals to the vertices of each finite volume triangular control volume. All FD schemes possess the property that the convected quantity is conserved on each control volume. In addition, the particular FD scheme used in this paper, the low diffusion B (LDB) scheme, is linearity preserving. High-order accuracy is achieved through a consistent treatment of the flux

and source terms in the constitutive equation. The use of a median-dual-cell (MDC) approach for the evaluation of flux and source terms is responsible for improved stability properties, interpreted in terms of maximum steady-state Weissenberg number solution attained.

The basis of the pure finite volume approach is a backward Euler scheme, with a semi-Lagrangian step to treat convection terms in both momentum and constitutive equations. This cell-centred finite volume scheme employs a staggered mesh. The discrete equations are solved using a generalisation of the SIMPLER scheme extended to include the treatment of the constitutive equation. The semi-Lagrangian component of the algorithm involves particle tracking to determine the location of control volumes at the previous time level, with a second-order area-weighting technique [30] to perform interpolation of the convected variable at this earlier time. Area-weighting schemes are inherently conservative when applied to conservation laws and provide improved stability response thereby. In addition, their use circumvents some of the problems generally associated with high-order upwinding schemes, traditionally implemented within the finite volume regime.

Comparison between these two alternative computational formulations has been reported previously in the literature. Accuracy and stability were investigated in [4] for the Oldroyd-B model, demonstrating spatial and temporal accuracy with reference to a model steady problem and the transient start-up of plane Poiseuille flow. The steady aspects of this work were extended more recently to the XPP model in a subsequent publication [1]. In the present article, we transcend the prediction of simple flows using traditional phenomenological models, to present an application of our finite volume schemes to kinetic theory models and the complex flow of a polymer melt through a 4:1 planar abrupt contraction. In this sense, a comparison is undertaken between the predictions of the FE/FV and SLFV schemes, focusing on the influence of model parameters on the velocity, stretch, and stress in the flow as a function of Weissenberg number. Particular emphasis is given to the growth and decay of salient-corner vortices as a function of Weissenberg number. In addition, we are able to cast some light upon the influence of inertia within the present context.

3.1. Hybrid finite element/finite volume scheme

The hybrid formulation incorporates fe-constructs for momentum-continuity and fv-cell-vertex stencils for stress. The underlying finite element structure is a time-splitting semi-implicit approach in which each time-step combines a three-stage structure. These stages consolidate the combination of two schemes: a Taylor–Galerkin scheme and an incremental pressure-correction scheme [13]. The diffusion terms in the momentum equation are treated in an implicit manner, in order to enhance stability. In the hybrid fe/fv context [41], we appeal to a cell-vertex finite volume (fv) approach to spatially discretise the stress in the constitutive equation, which appears at discrete Stage 1 of the formulation. The current hybrid implementation, extended to include the XPP-model, integrates the *fv*-scheme (for stress) within that of the *fe*-backbone (for velocity and pressure). This forms four *fv*-triangular-subcells per parent *fe*-triangle, see Fig. 2a.

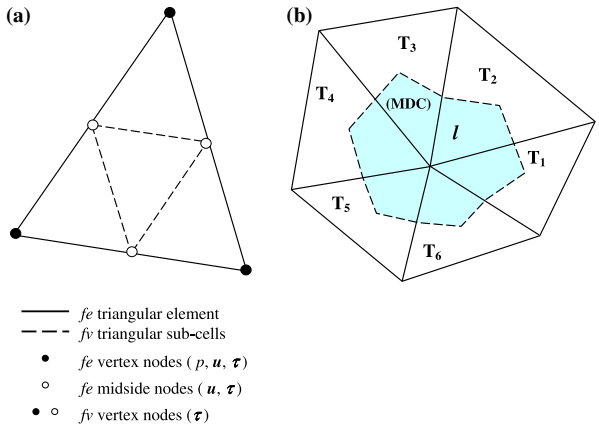

Fig. 2. FE/FV spatial discretisation: (a) *fe*-cell with four *fv* sub-cells and FD per T, (b) *fv*-control volume for node *l*, with median-dual-cell (MDC-shaded).

We proceed to summarise the hybrid finite volume methodology utilised here for the pom–pom equations, identifying flux $\mathbf{R} = (R)_{ij} = \mathbf{u} \cdot \nabla\boldsymbol{\tau}$ and source $\mathbf{Q} = (Q)_{ij}$ as

$$\mathbf{Q} = \frac{1}{We}[2(1-\beta)\boldsymbol{d} - f(\lambda,\tau)\tau] - \frac{1-\beta}{(We)^2}[f(\lambda,\tau)-1]\boldsymbol{I} - \frac{\alpha}{1-\beta}\tau\cdot\tau + (\nabla\mathbf{u})^{\dagger}\cdot\boldsymbol{\tau} + \boldsymbol{\tau}\cdot(\nabla\mathbf{u}). \tag{7}$$

In component form, the stress nodal-update is based upon a cell-vertex fluctuation-distribution (FD) procedure (upwinding) on each *fv*-subcell T_i, combined with a contribution from a median-dual-cell (MDC) sub-area, see Fig. 2b. The FD-procedure adopts FD-coefficients α_l^T, which assign products of flux (R_T, non-conservative form [5]) and source (Q_T) discrete cell (T_i) residuals to the vertices (l) of each *fv*-triangle T_i (Ω_{T_i}, of area Ω_T), according to an upwinding strategy. For this purpose and in the steady-state regime, we retain the linearity preserving Low-Diffusion B, LDB-scheme, designed to minimise numerical diffusion. The MDC contribution appends a uniform distribution of $R^l_{\mathrm{MDC^T}}$ and $Q^l_{\mathrm{MDC^T}}$, to node l within T_i, from its associated MDC control volume ($\Omega_l^{T_i}$, of area $\hat{\Omega}_l$). In order to ensure consistency through time discretisation in a stringent manner (see [41]), we examine separately FD and MDC stress nodal updates. Consequently, these distinct contributions are blended together using solution dependent parameters δ_T and δ^T_{MDC}. After summation over all *fv*-subcells T_l surrounding node l, we derive our proposed scheme over a single time-step Δt for the solution increment $\Delta\tau_l^{n+1}$, where $\Delta\tau_l^{n+1} \equiv (\tau^{n+1} - \tau^n)_l$,

$$\left[\sum_{\forall T_l}\Omega_{T_i}\delta_T\alpha_l^T + \sum_{\forall \mathrm{MDC}_l}\delta^T_{\mathrm{MDC}}\Omega_l^{T_i}\right]\frac{\Delta\tau_l^{n+1}}{\Delta t} = \sum_{\forall T_l}\delta_T\alpha_l^T b^T + \sum_{\forall \mathrm{MDC}_l}\delta^T_{\mathrm{MDC}}b^l_{\mathrm{MDC^T}}, \tag{8}$$

utilising the cryptic notation $b^T = (R_T + Q_T)$ and $b^l_{\mathrm{MDC^T}} = (R^l_{\mathrm{MDC^T}} + Q^l_{\mathrm{MDC^T}})$. Area-sums on the left-hand side of (8) are reminiscent of the ideas of Hubbard and Roe [21] for pure convection problems. The parameter δ_T is defined as: $\delta_T = \xi/3$ if $|\xi| \leqslant 3$ and 1 otherwise [40]. Here, $\xi = We(a/h)$, where a represents the magnitude of an average advection-velocity within each *fv*-cell T, and h the square-root of the area of that *fv*-cell. There are two new important aspects in this nodal-update: *first*, the consistent distribution of flux and source terms, both under fluctuation-distribution and MDC; *second*, the arealess nature of the resultant equation that reflects consistency in area-weighting. Furthermore, a linked and dynamic MDC weighting parameter of the form $\delta^T_{\mathrm{MDC}} = 1 - \delta_T$ has proved promising. This ensures that the relative strength of flux and source terms is reflected, through FD and MDC contributions to the stress nodal update. We may point to further more recent embellishments upon these formulation ideas under alternative application settings, in the true transient context [42] and in the mildly-compressible regime [19].

3.2. Semi-Lagrangian Finite Volume (SLFV) scheme

The semi-Lagrangian finite volume scheme is a cell-centred finite volume method for discretising the governing equations in general conservative form. A reference grid is superimposed upon the computational

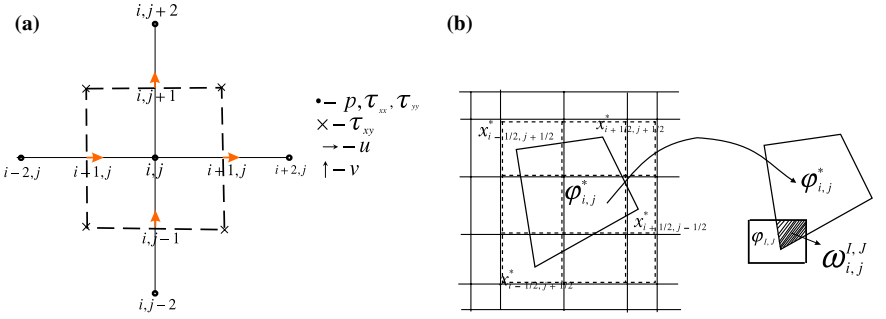

Fig. 3. SLFV: (a) location of the variables on the finite volume grid, (b) formation of the departure cell $C^*_{i,j}$ using the particle-following transformation to determine the vertices.

domain and a control volume is associated with each unknown on the grid (Fig. 3), as in [30]. An operator splitting technique is employed to discretise the governing equations in time. The convection terms in the momentum and constitutive equations are treated using a semi-Lagrangian technique based on a particle tracking method, involving the solution of pure convection problems at each time-step to obtain intermediate values of the velocity ($\mathbf{u}^*$) and extra-stress ($\boldsymbol{\tau}^*$). This is followed by the solution of an unsteady generalised Stokes problem to determine the pressure and updated velocity

$$Re\left(\frac{\mathbf{u}^{n+1}-\mathbf{u}^{*n}}{\Delta t}\right)-2\beta\mathbf{d}^{n+1}+\nabla p^{n+1}=\nabla\cdot\boldsymbol{\tau}^{n}, \tag{9}$$

$$\nabla\cdot\mathbf{u}^{n+1}=0, \tag{10}$$

and the solution of an unsteady problem to update the stress, of pom–pom form,

Table 1
Mesh characteristics parameters, FE/FV and SLFV

Meshes	Elements/volumes	Nodes	Degrees of freedom $(\boldsymbol{u},p,\boldsymbol{\tau})$	$R_{\min}$
m1 (FE/FV)	980	2105	13,193	0.0243
m2 (FE/FV)	1542	3279	20,543	0.019
m3 (FE/FV)	2987	6220	38,937	0.0063
M1 (SLFV)	2240		26,880	0.10
M2 (SLFV)	3200		38,400	0.09
M3 (SLFV)	3600		43,200	0.08
M4 (SLFV)	7200		86,400	0.04

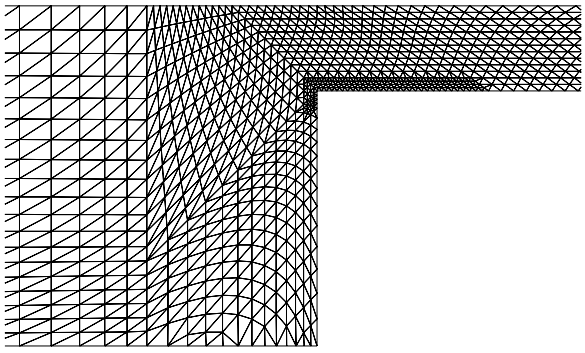

Fig. 4. Unstructured FE/FV meshing (m3), in contraction zone.

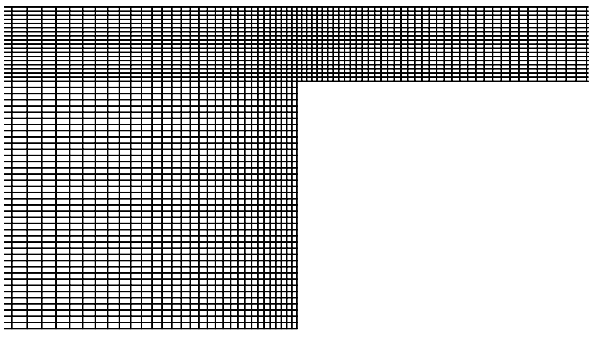

Fig. 5. Structured SLFV mesh (M4) in contraction zone.

$$We\left(\frac{\boldsymbol{\tau}^{n+1}-\boldsymbol{\tau}^{*n}}{\Delta t}\right)+f(\lambda^n,\boldsymbol{\tau}^n)\boldsymbol{\tau}^{n+1}+\frac{\alpha We}{1-\beta}\boldsymbol{\tau}^n\cdot\boldsymbol{\tau}^n=2(1-\beta)\mathbf{d}^n-\{f(\lambda^n,\boldsymbol{\tau}^n)-1\}\frac{1-\beta}{We}\mathbf{I}. \tag{11}$$

The SIMPLER algorithm [28] is used within the first stage of this process to ensure that a divergence-free velocity field is obtained.

Convection is treated using the semi-Lagrangian cell-centred method as described by Phillips and Williams [30]. Particles arriving at the four corner points of a rectangular control volume $C_{i,j}$ associated with the dependent variable ϕ are retraced to a previous time-step where the departure points define a deformed volume, $C^{*n}_{i,j}$,

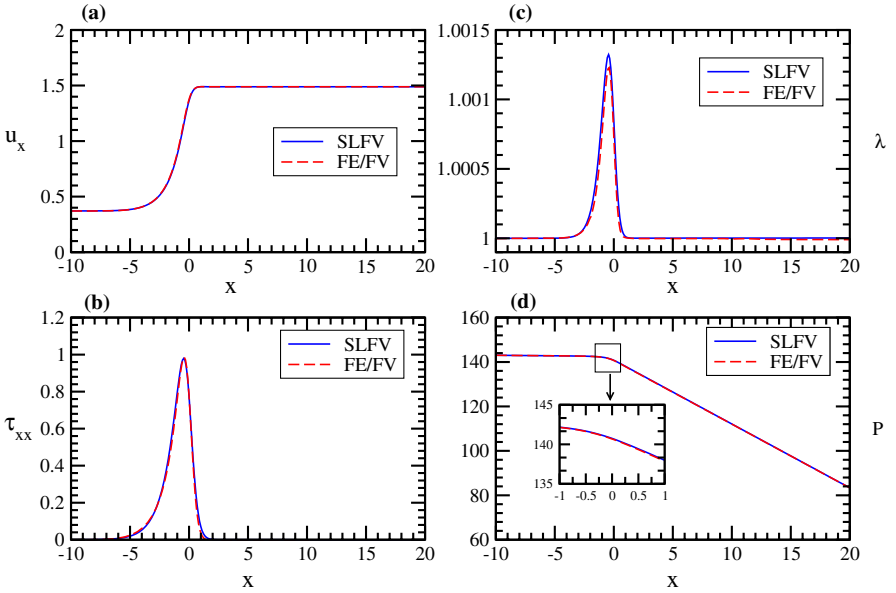

Fig. 6. Symmetry line flow results; $We = 0.1$, $Re = 0$.

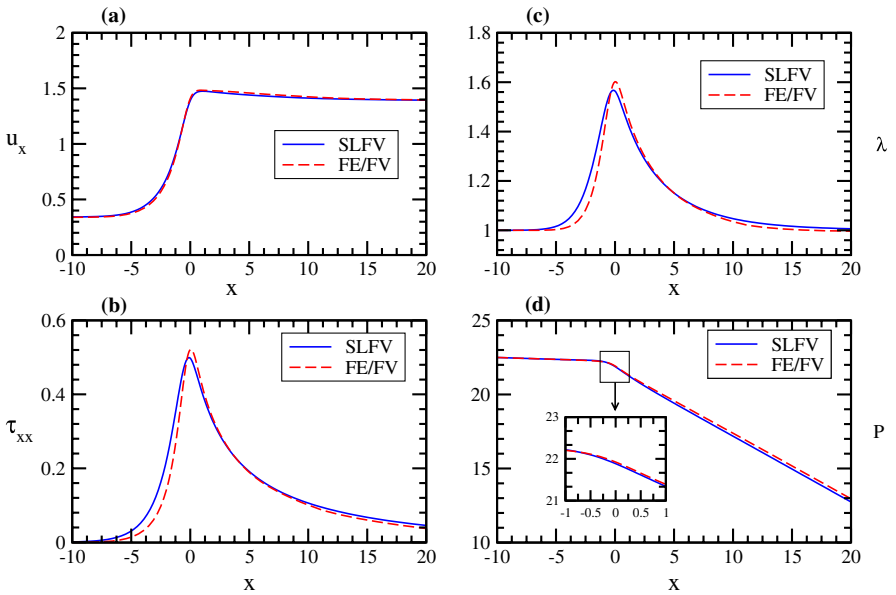

Fig. 7. Symmetry line flow results; $We = 10$, $Re = 0$.

formed by joining the departure points with straight line segments (Fig. 3). Within each cell, $C_{i,j}$, and at time $t_n = n\Delta t$, the cell-average approximation to $\phi^n_{i,j}$ of $\phi(x, y, t_n)$ is evaluated, viz.

$$\phi^n_{i,j} \approx \frac{1}{\Delta x_i \Delta y_j} \int \int_{C_{i,j}} \phi(x, y, t_n)\, \mathrm{d}x\, \mathrm{d}y, \tag{12}$$

where $\Delta x_i = x_{i+\frac{1}{2}} - x_{i-\frac{1}{2}}$, $\Delta y_j = y_{j+\frac{1}{2}} - y_{j-\frac{1}{2}}$. The departure points at time $t = t_n$ are determined utilising a particle tracking transformation. The approximation of cell-average values is performed by means of an area-weighting technique that uses a weighted sum of the values of ϕ^n over those control volumes of the reference grid which overlap with cell $C^{*n}_{i,j}$. The second-order area-weighting scheme to compute $\phi^{*n}_{i,j}$ adopts the form

$$\phi^{*n}_{i,j} = \frac{1}{\Delta x_i \Delta y_j} \underbrace{\sum}_{I,J \in Z} \left[\omega^{I,J}_{i,j} (\phi^n_{I,J} - \alpha^n_{I,J} \bar{x}_{I,J} - \beta^n_{I,J} \bar{y}_{I,J}) + \int \int_{C^{*n}_{i,j} \cap C_{I,J}} (\alpha^n_{I,J} x + \beta^n_{I,J} y)\, \mathrm{d}x\, \mathrm{d}y \right], \tag{13}$$

where $\omega^{I,J}_{i,j}$ is the common area between $C^{*n}_{i,j}$ and $C_{I,J}$, Z is the set of indices of all points in the computational domain and $\alpha_{i,j}$ and $\beta_{i,j}$ are central difference approximations to the fluxes.

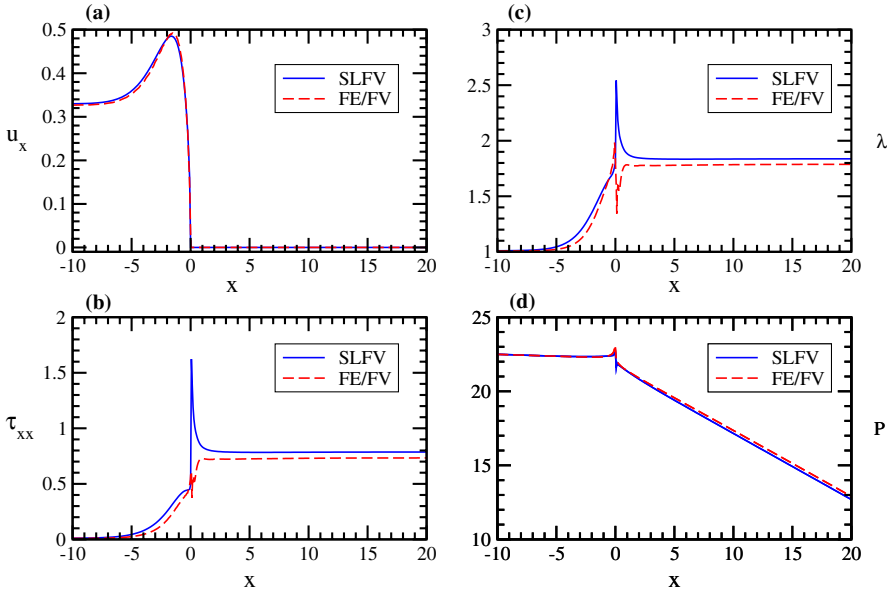

Fig. 8. Profiles along downstream wall, $y = 3$; $We = 10$, $Re = 0$.

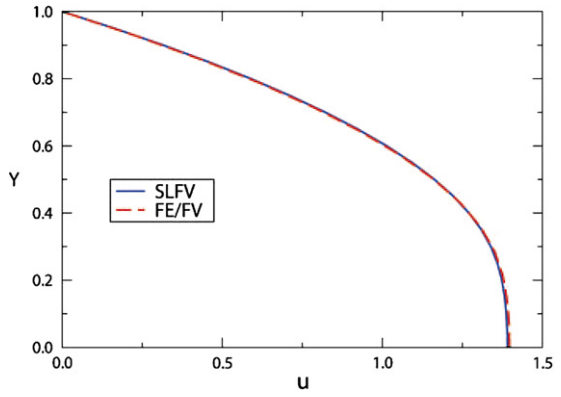

Fig. 9. Velocity profile at downstream wall location $x = 20$, $We = 10$, $Re = 0$.

4. Flow through a 4:1 planar contraction

4.1. Problem specification

The benchmark problem of flow through a 4:1 planar contraction is considered. Fluid passes from one channel into another of smaller cross-sectional width and in the process generates a complex flow exhibiting

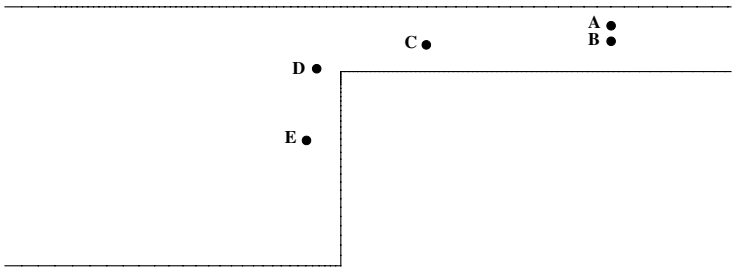

Fig. 10. Sample points used in the 4:1 contraction domain.

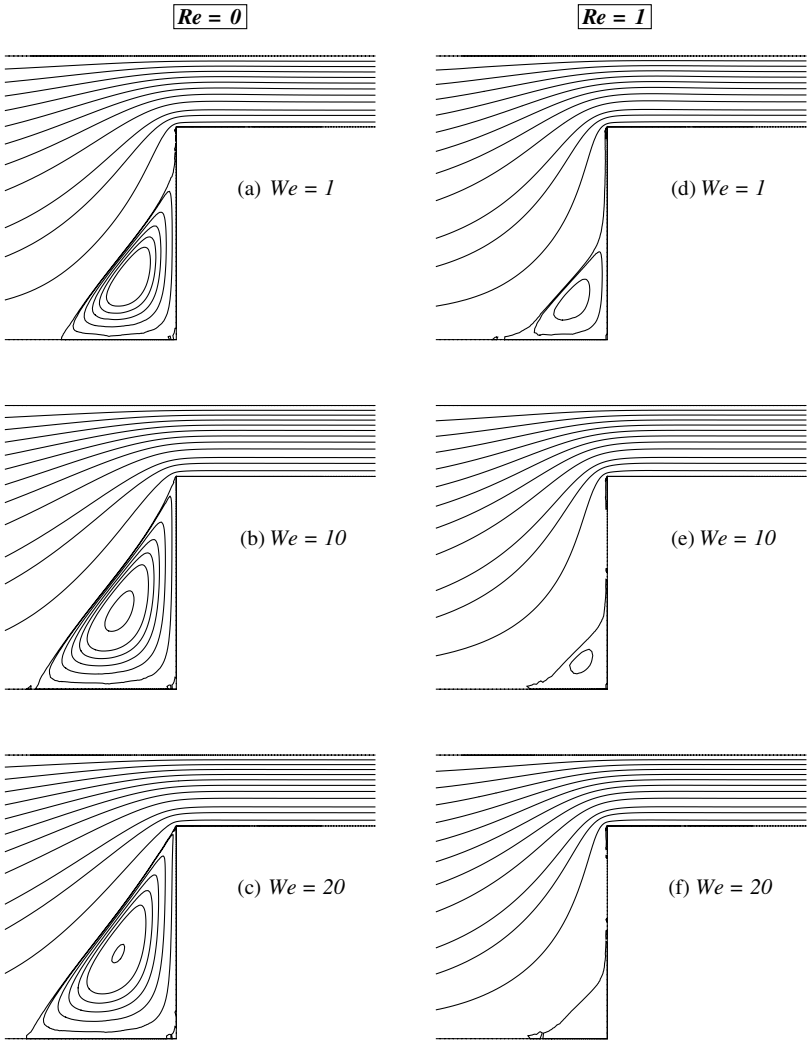

Fig. 11. Stream function with increasing We, $Re = 0$ and 1.

regions of strong shearing near the walls and planar extension along the centreline (centre plane). The length of upstream and downstream are $27.5L$ and $49L$, respectively.

To solve the governing system of partial differential equations for the XPP model it is necessary to impose suitable boundary and initial conditions. However, unlike the situation for UCM/Oldroyd-B models analytical expressions for fully-developed velocity and extra-stress XPP-profiles are not readily available. Instead, such profiles must be determined computationally (see [1], for details), by solving the equivalent planar entry-channel flow problem. Fully developed boundary conditions are established at the outflow ensuring no change with respect to velocity component U_x and vanishing component U_y. No-slip boundary conditions are imposed along the stationary walls.

We are able to contrast the alternative numerical solutions obtained with the two FV-schemes described above, commenting upon predictions for the XPP model within the 4:1 planar contraction flow. A series of meshes is used for both methods to ensure spatial convergence. Mesh characteristics are provided in Table 1, detailing numbers of elements (FE/FV) or volumes (SLFV), total numbers of degrees of freedom and smallest mesh spacing employed. The SLFV scheme invokes a structured rectangular mesh on which the grid point spacing follows a geometric progression as one moves away from the re-entrant corner in the horizontal direction. In Figs. 4 and 5, we display the finest meshes used with FE/FV and SLFV schemes. The FE/FV mesh (m3) is an

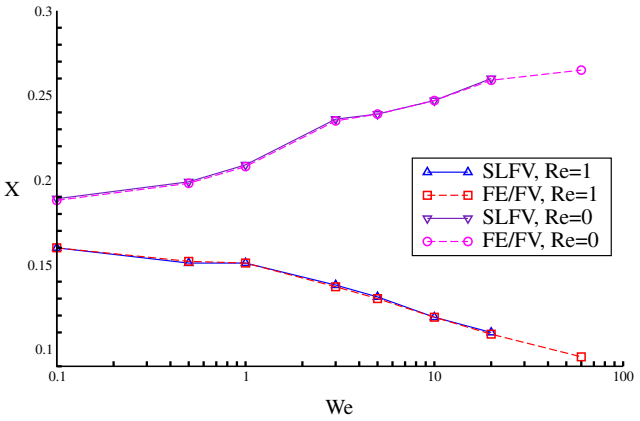

Fig. 12. Salient-corner vortex cell-size; trends with increasing We, $Re = 0$ and 1.

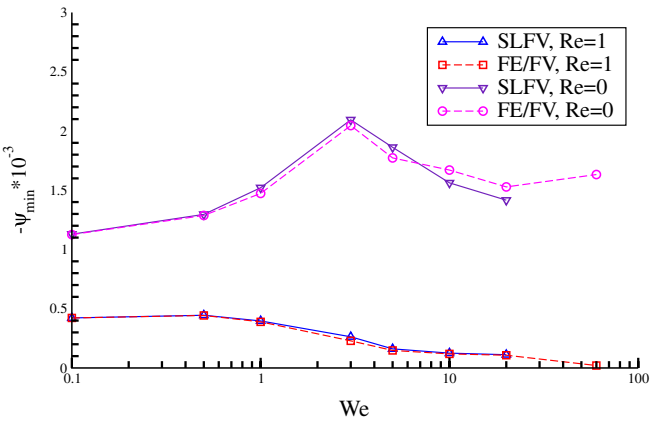

Fig. 13. Salient-corner vortex intensity ($\times 10^{-3}$); trends with increasing We, $Re = 0$ and 1.

Table 2
Mesh convergence: salient-corner vortex cell-size (X), $0.1 \leqslant We \leqslant 20$ and $Re = 0$

We	FE/FV			SLFV	
	m1	m2	m3	M3	M4
0.1	0.185	0.188	0.188	0.189	0.189
0.5	0.192	0.198	0.198	0.199	0.199
1.0	0.206	0.208	0.208	0.209	0.209
3.0	0.230	0.234	0.235	0.230	0.236
5.0	0.236	0.239	0.239	0.239	0.239
10.0	0.242	0.247	0.247	0.247	0.247
20.0	0.255	0.259	0.259	0.259	0.260

Table 3
Mesh convergence: salient-corner vortex cell-size (X), $0.1 \leqslant We \leqslant 20$ and $Re = 1$

We	FE/FV			SLFV			
	m1	m2	m3	M1	M2	M3	M4
0.1	0.163	0.160	0.160	0.162	0.161	0.161	0.160
0.5	0.154	0.152	0.152	0.153	0.152	0.152	0.152
1.0	0.153	0.151	0.151	0.153	0.152	0.151	0.151
3.0	0.139	0.137	0.137	0.139	0.139	0.138	0.138
5.0	0.133	0.130	0.130	0.134	0.133	0.131	0.131
10.0	0.122	0.119	0.119	n/a	n/a	0.119	0.119
20.0	0.113	0.109	0.109	n/a	n/a	0.110	0.110

Table 4
Mesh convergence: salient-corner vortex intensity ($-\psi \times 10^{-3}$), $0.1 \leqslant We \leqslant 20$ and $Re = 0$

We	FE/FV			SLFV	
	m1	m2	m3	M3	M4
0.1	1.125	1.126	1.126	1.129	1.129
0.5	1.285	1.286	1.287	1.296	1.298
1.0	1.472	1.472	1.473	1.521	1.523
3.0	2.044	2.045	2.046	2.094	2.098
5.0	1.770	1.771	1.773	1.862	1.864
10.0	1.668	1.669	1.670	1.562	1.563
20.0	1.520	1.521	1.528	1.416	1.418

Table 5
Mesh convergence: salient-corner vortex intensity ($-\psi \times 10^{-3}$), $0.1 \leqslant We \leqslant 20$ and $Re = 1$

We	FE/FV			SLFV			
	m1	m2	m3	M1	M2	M3	M4
0.1	0.410	0.412	0.422	0.441	0.439	0.423	0.422
0.5	0.408	0.428	0.443	0.450	0.448	0.446	0.445
1.0	0.318	0.338	0.389	0.412	0.401	0.399	0.397
3.0	0.201	0.218	0.229	0.271	0.268	0.263	0.262
5.0	0.138	0.140	0.148	0.164	0.162	0.161	0.161
10.0	0.102	0.112	0.119	n/a	n/a	0.125	0.124
20.0	0.101	0.103	0.107	n/a	n/a	0.112	0.111

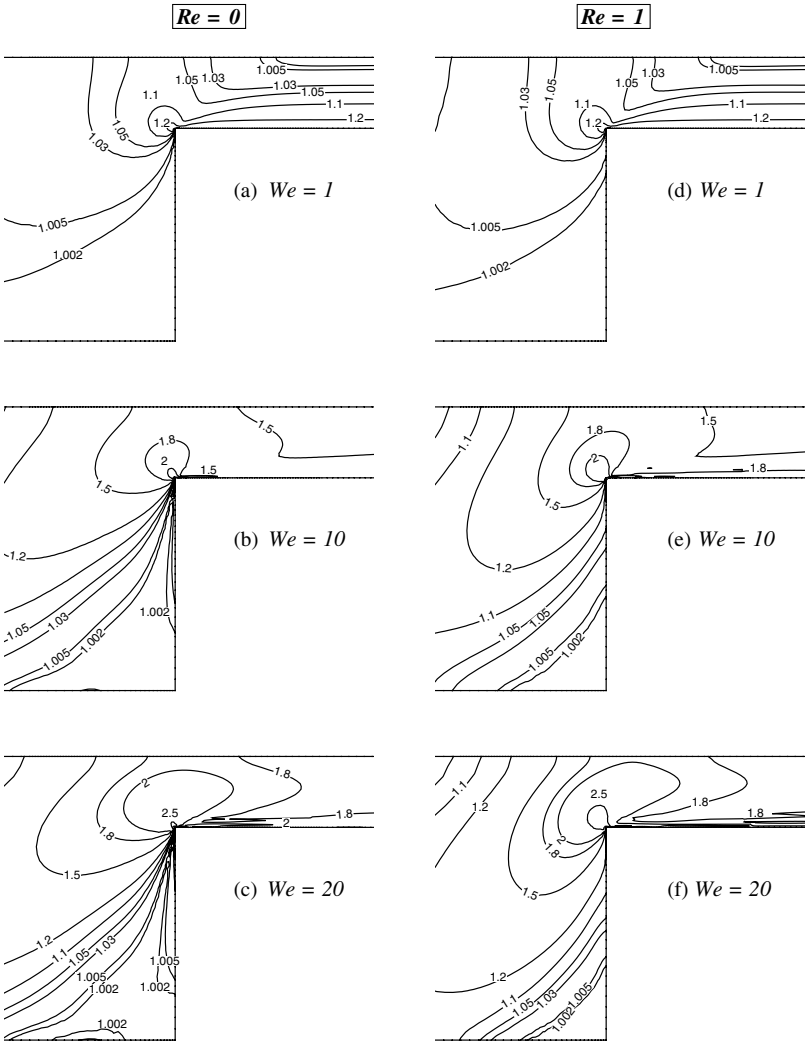

Fig. 14. Backbone stretch, (λ) fields: increasing We, $Re = 0$ and 1.

unstructured mesh that allows for a finer discretisation around the re-entrant corner, whilst the SLFV mesh (M4) is a rectangular non-uniform structured mesh. A basis for comparison across schemes and structure may be established via stress degrees of freedom over comparable control volume zones. In this respect, a single rectangle in the pure FV scheme forms two triangular subcells of the hybrid scheme.

4.2. Numerical results

Advancing upon our earlier studies [1,4], computations have been performed for one particular set of XPP parameters, namely: $\epsilon = 1/3$, $q = 2$, $\alpha = 0.15$ and $\beta = 1/9$. Here, to accommodate for inertial influence, we have considered two levels of Reynolds number, viz. $Re = 0$ and 1. Comparable computations across schemes have been performed for Weissenberg numbers in the range $0 \leqslant We \leqslant 20$.[2] Time-step termination is ensured when the L_2-norm relative maximum difference between solution approximations over two successive time

[2] Solutions for FE/FV have been gathered up to $We = 60$.

nitiated from a $We = 0.1$ solution state and con-
ions at stages $We = 0.5$, 1, 3, 5, 10 and 20.
ntal velocity component, stretch, polymeric nor-
$= 10$, respectively. The contraction is located at
which is rather weak at $We = 0.1$. The backbone
ontraction plane when $We = 0.1$. Relaxation is
al stress has not reached its fully-developed level
se agreement observed between results for each
$= 10$. This is within acceptable error bars due
red versus structured meshing; variable location,
quadratic FE-interpolation. The FE/FV scheme
e SLFV scheme. The peak value of τ_{xx} is lower
. This is a clear manifestation of strain-softening
. 8 profiles along the downstream wall where the
ment around the corner due to the discretisation

differences referred to above. In Fig. 9, we display the velocity profile at the downstream section $x = 20$ for $We = 10$ and $Re = 0$. Excellent agreement is obtained between predictions for the two schemes.

Turning to the stream function, contour fields are provided in Fig. 11 for $Re = 0$ and 1, covering Weissenberg numbers in the range $0 \leqslant We \leqslant 20$. The dimensionless salient-corner vortex size, X, is defined by

$$X = L_v/2L_u,$$

where L_v is the distance along the upstream channel-wall of the separation point from the salient corner, and L_u is the upstream channel half-width. For creeping flow, X gradually grows with increasing We (see Fig. 12). This agrees with the findings of Bishko et al. [9] in computations with the differential approximation to the original pom–pom model. Simultaneously, the intensity of the vortex increases up to $We = 3$, thereafter, decreasing monotonically (see Fig. 13). This behaviour may be explained in terms of the initial moderate strain-hardening of the XPP model, followed by some strain-softening. Here, we relate this response to that of the exponential PTT model with $\varepsilon = 0.25$ (see [2,3]). In contrast, one notes that the Oldroyd-B model (or PTT with $\varepsilon = 0.02$) displays extreme strain-hardening, even at moderate extension rates (spurning lip-vortices and subsequently reducing critical We). Sustained salient-corner vortex growth is consistent with decreasing

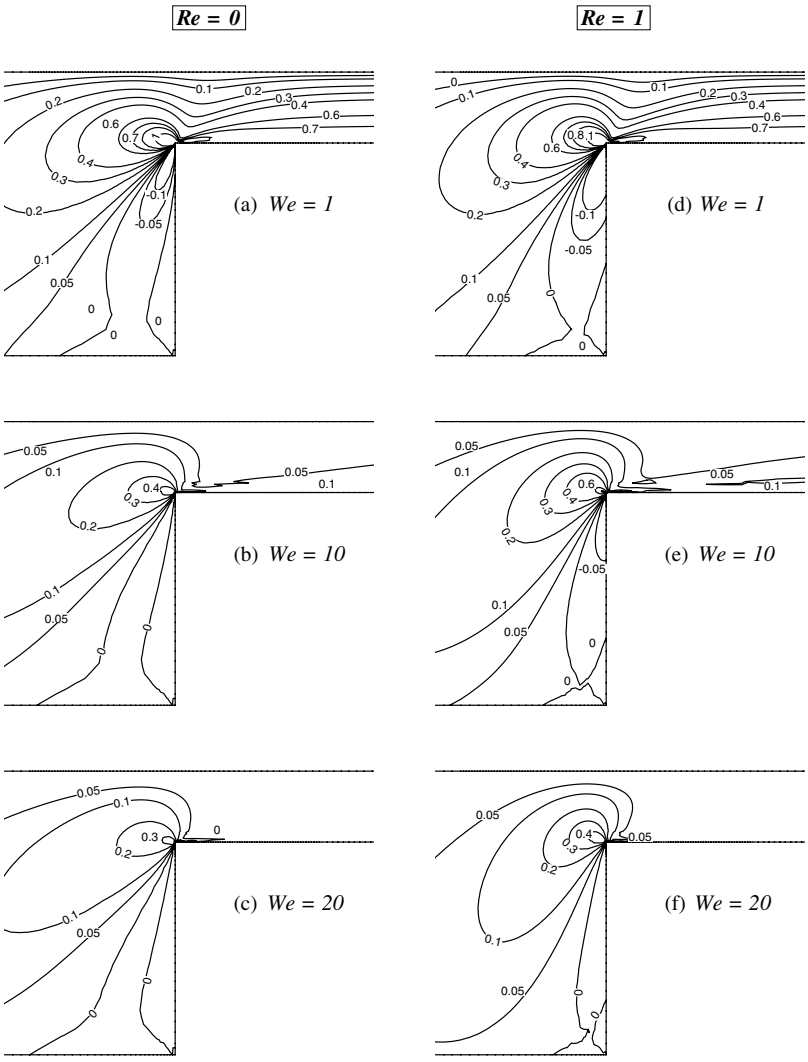

Fig. 16. Shear stress (τ_{xy}) fields: increasing We, $Re = 0$ and 1.

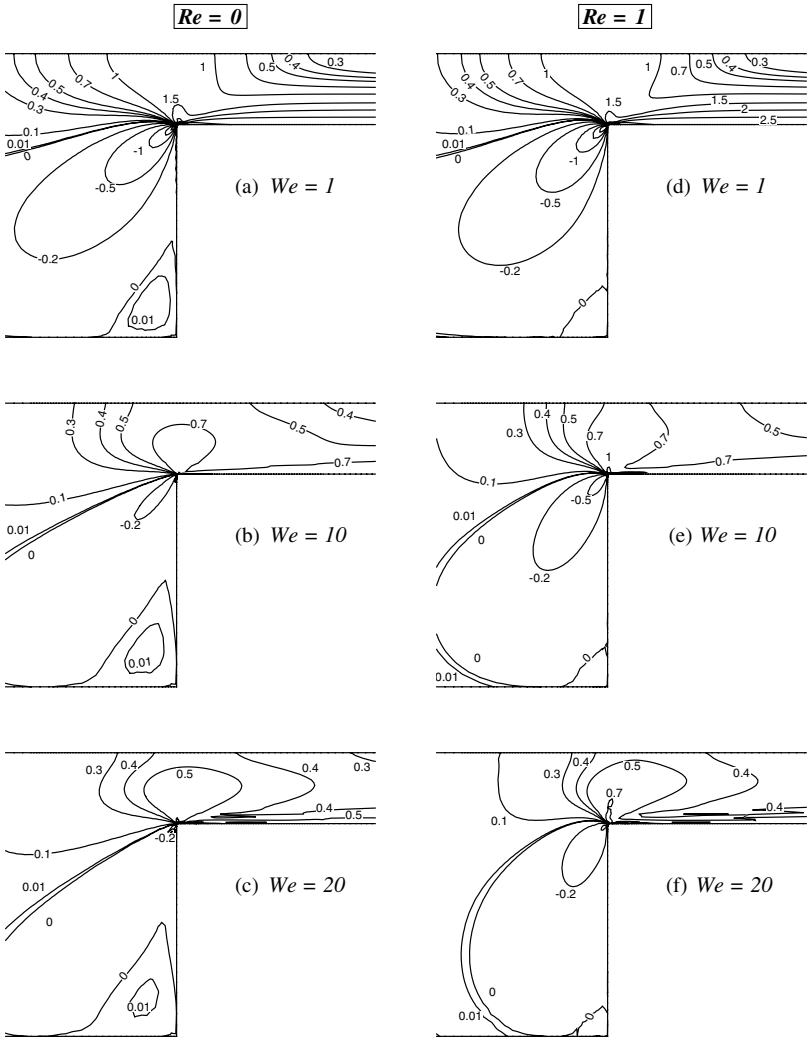

Fig. 17. First normal stress difference (N_1) fields: increasing We, $Re = 0$ and 1.

Trouton ratios as We increases. Again, predictions for salient-corner vortex cell-size and intensity, generated with the two independent finite volume schemes for the XPP model, are found to be in excellent agreement. Under such moderate strain-hardening, no lip-vortex activity is detected, as consistent with LPTT ($\varepsilon = 0.25$) of Carew et al. [12] and pom–pom results of Bishko et al. [9].

With the introduction of inertia, we can discern vortex reduction with increasing Weissenberg number. This lies in dramatic contrast to the situation for creeping flow (see Fig. 12), where the vortex grows steadily in size with increasing Weissenberg number. So, for $Re = 1$, increasing elasticity suppresses the salient-corner vortex. Initially, the intensity of the salient-corner vortex slightly increases up to $We = 0.5$, before decreasing monotonically (see Fig. 13). For a direct comparison at $We = 20$, the intensity of the salient-corner vortex is approximately 10% of its value for the corresponding creeping flow situation.

Quantitative information regarding mesh convergence of the salient-corner vortex cell-size and intensity[3] is provided in Tables 2–5 for $Re = 0$ and 1, respectively, covering the range $0.1 \leqslant We \leqslant 20$. The information in these tables demonstrates that convergence with mesh refinement has been achieved for the range of param-

[3] Salient-corner vortex intensity is reported on maximum stream function values scaled by 10^{-3}.

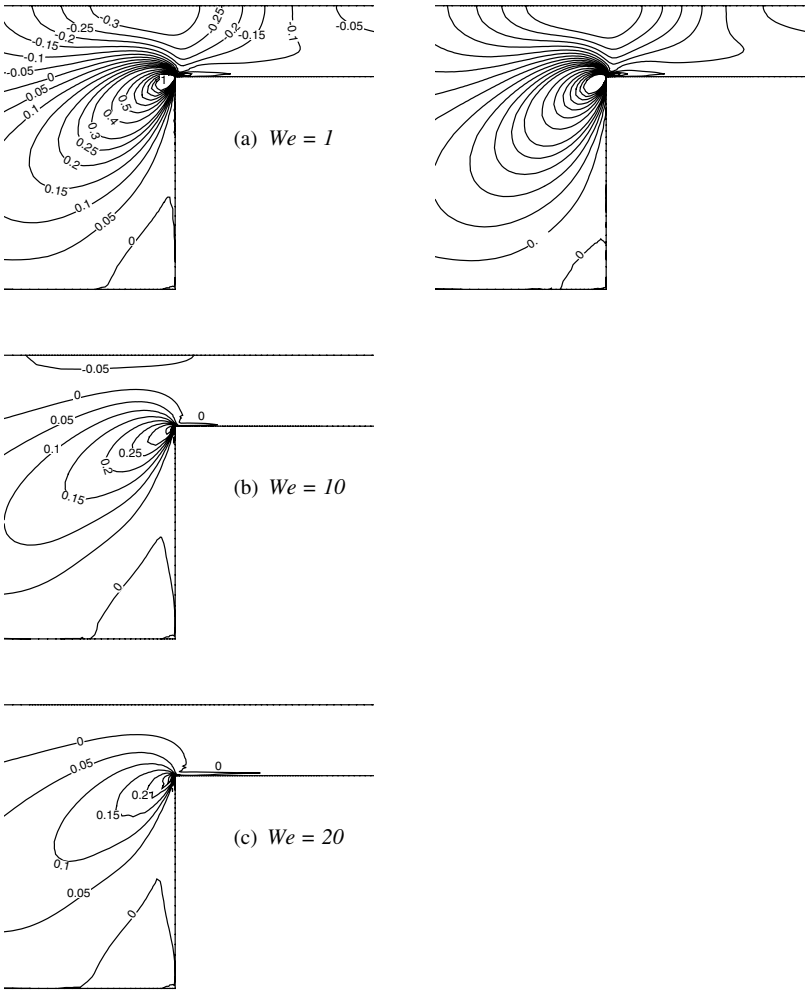

eters considered. An interesting feature of computation with the pom–pom model is that, for larger values of Weissenberg number, the computational mesh must be sufficiently fine in order to sustain a suitably converged solution. This goes hand-in-hand with model expectations, as for large Weissenberg number, the pom–pom stress becomes Newtonian once more with the solvent contribution dominating (see Fig. 1).

Bishko et al. [9] have shown that the inflow section can be divided into three regions, two zones of relatively unstretched material, one near the centreline and one in the recirculating vortex. The third banded region is one of highly-stretched material. This feature can be observed for creeping flow in Fig. 14 for $We = 1$, 10, and 20.[4] Regions of larger stretch develop around the re-entrant corner and along the downstream wall as the Weissenberg number increases. The banded region of more stretched material corresponds to the deformation-rates in which extensional effects dominate over shear effects (see Fig. 1d). Note that, when $We = 20$, stretch near the re-entrant corner locally exceeds a level of two, which is greater than the number of branched-arms, q. In the original pom–pom model this would not have been possible due to its inherent con-

[4] All field contour plots are practically identical for both schemes, Figs. 13–20; the choice here is to display those for FE/FV scheme.

straint that stretch could not exceed the number of arms. In the present circumstance, this constraint has been removed within the XPP model.

The associated developing polymeric stress field structure may be gathered through the normal component (τ_{xx}) of Fig. 15 and the shear component (τ_{xy}) of Fig. 16. In contrast to the stretch, which still increases with increasing Weissenberg number, the normal stress component τ_{xx} relaxes at higher values of *We*, particularly around the re-entrant corner. This feature of the XPP model was also observed in start-up planar channel Poiseuille flow [35]. In Fig. 16, we observe a general decrease in the magnitude of τ_{xy} with increasing *We* in the banded zone, where extensional flow dominates that of shear.

The behaviour of the first normal stress difference, N_1, shown in Fig. 17, follows that in τ_{xx}, and is in keeping with the extensional rheology plots. N_1 reduces in magnitude as *We* increases across the domain around the re-entrant corner zone in particular. This is a consequence of strain-softening (see below). The second normal stress difference, N_2, is non-zero in these complex flows with this XPP model ($\alpha \neq 0$). N_2-fields convey the curvature structure and growth of the evolving salient-corner vortex as *We* increases, noting the difference between inertial settings ($Re = 0$ and 1) (see Fig. 18). The d_{xx} and d_{xy} components of the rate-of-deformation

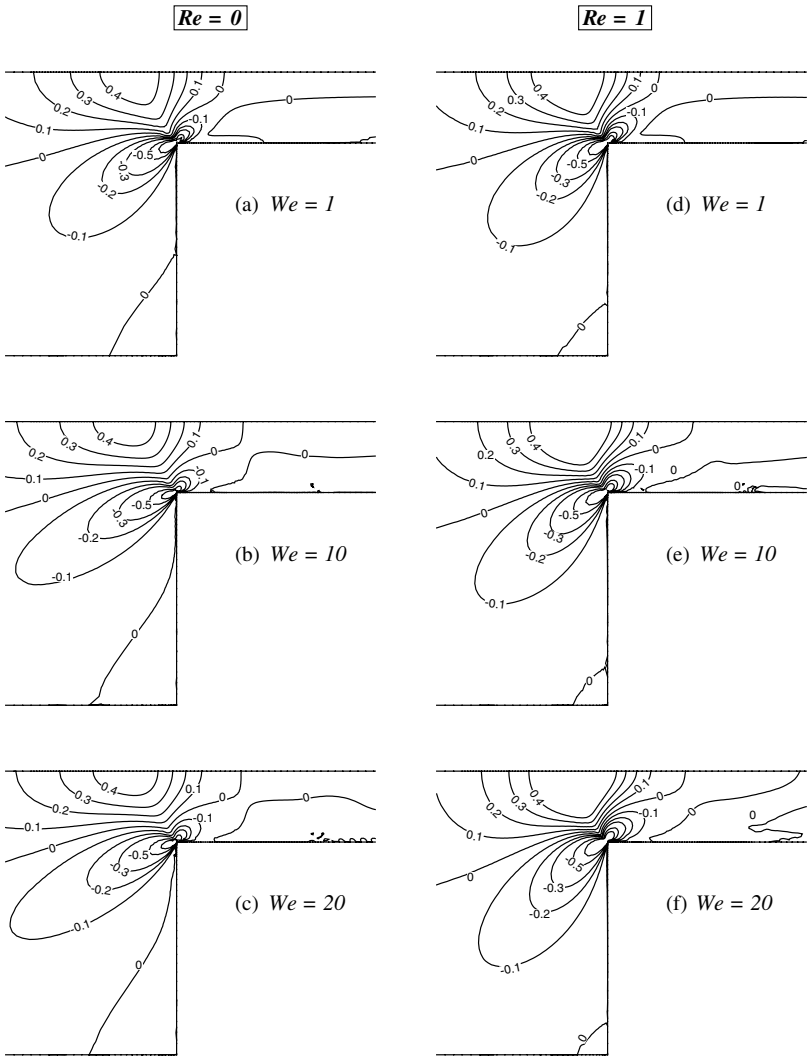

Fig. 19. Rate-of-strain (d_{xx}) fields: increasing *We*, $Re = 0$ and 1.

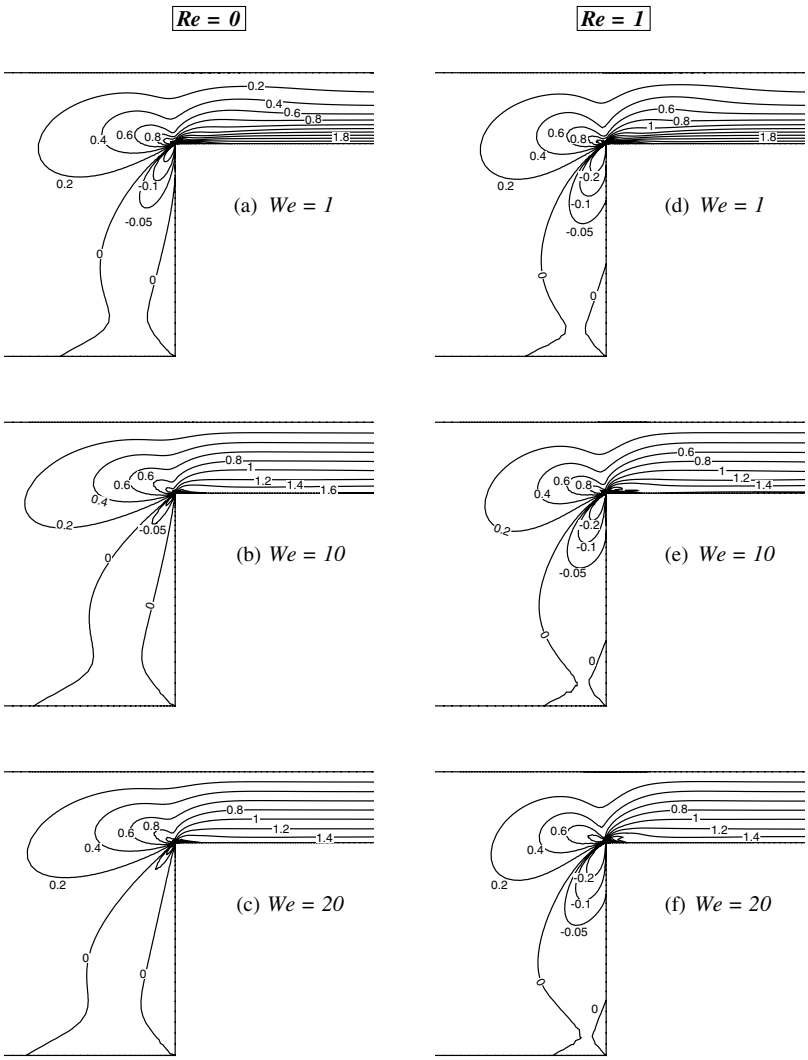

Fig. 20. Rate-of-strain (d_{xy}) fields: increasing We, $Re = 0$ and 1.

tensor are shown in Figs. 19 and 20, respectively. The component d_{xx} is largely unaffected by increase in We. Conspicuously, regions of largest stretch (λ) in the entry zone correspond to similar zones in extension-rate, d_{xx}. Similarly, d_{xy} is also unaffected with increase in We, with the exception of along the downstream wall where a boundary layer in stress develops. In addition, Fig. 21 presents principle stress difference field patterns ($\tau_{\mathrm{PSD}} = \sqrt{4\tau_{xy}^2 + N_1^2}$). Here, in accordance with the finding of Verbeeten et al. [38], we observe similar "butterfly" shaped fringes and the recirculation zone upstream of the contraction. A quantitative summary of the values of stretch (λ) and first normal stress difference (N_1) is provided in Table 6. These data cover the field plots and apply for both FE/FV and SLFV schemes at the various sample points indicated, A–E of Fig. 10. The agreement through schemes and We-setting is uniform across the point sampling, being of O(1%) in each variable within the maximum norm, in relative difference between the scheme solutions per variable[5].

[5] Definition: $\frac{\|x_1 - x_2\|_\infty}{\|x\|_\infty}$ variable x_i, scheme $i = 1, 2$.

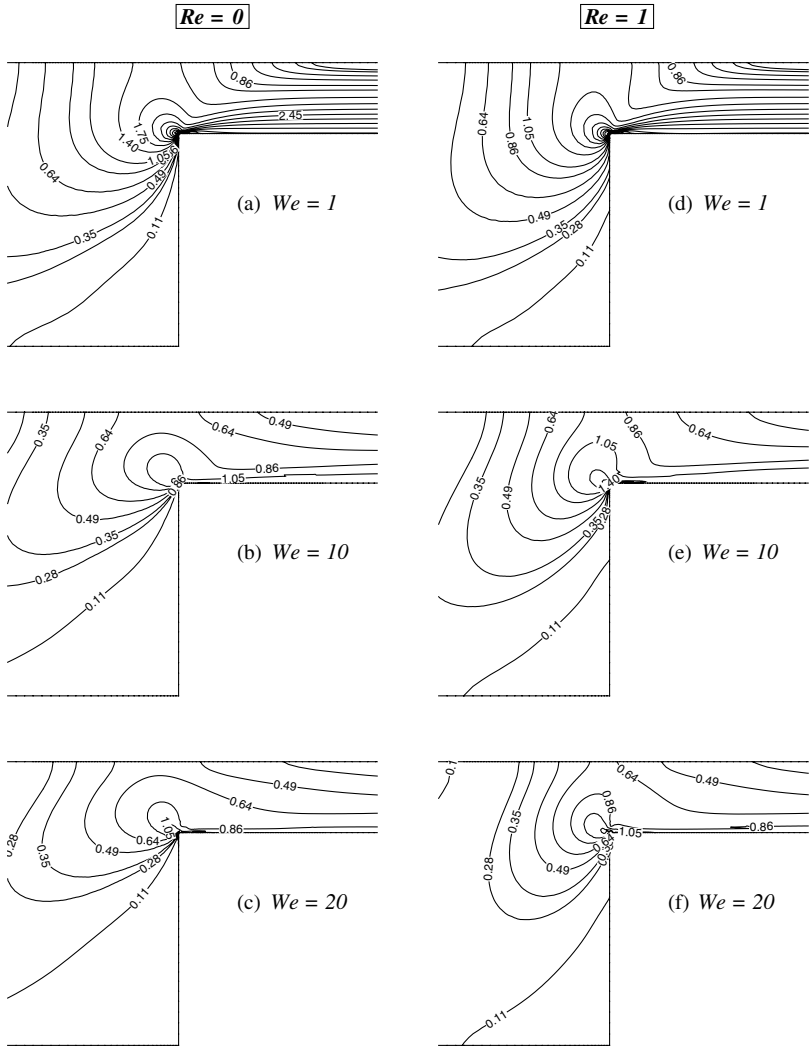

Fig. 21. Fringe pattern fields: increasing *We*, $Re = 0$ and 1.

Table 6
Values of stretch (λ) and first normal stress difference (N_1) at sample points, $0.1 \leqslant We \leqslant 20$, $Re = 0$ (contraction point at $x = 0.0$, $y = 3.0$)

Sample-points	*We*	FE/FV			SLFV		
		1	10	20	1	10	20
A	λ	1.01	1.16	1.35	1.01	1.18	1.35
($x = 19.9$, $y = 3.78$)	N_1	0.13	0.22	0.20	0.14	0.23	0.20
B	λ	1.05	1.50	1.72	1.06	1.55	1.71
($x = 19.9$, $y = 3.50$)	N_1	0.76	0.53	0.37	0.81	0.58	0.37
C	λ	1.05	1.49	1.65	1.06	1.55	1.71
($x = 9.99$, $y = 3.50$)	N_1	0.76	0.52	0.34	0.81	0.57	0.37
D	λ	1.01	1.26	1.45	1.01	1.36	1.55
($x = -1.94$, $y = 3.07$)	N_1	0.24	0.21	0.18	0.25	0.27	0.21
E	λ	1.01	1.23	1.41	1.01	1.26	1.39
($x = -2.00$, $y = 2.07$)	N_1	−0.23	0.044	0.015	−0.19	0.026	0.049

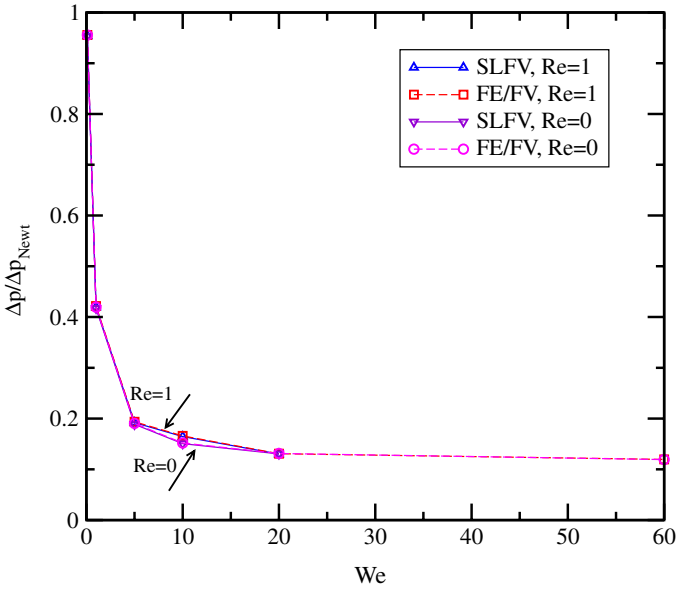

Fig. 22. Pressure-drop vs. We: SLFV and FE/FV schemes; $Re = 0$ and 1.

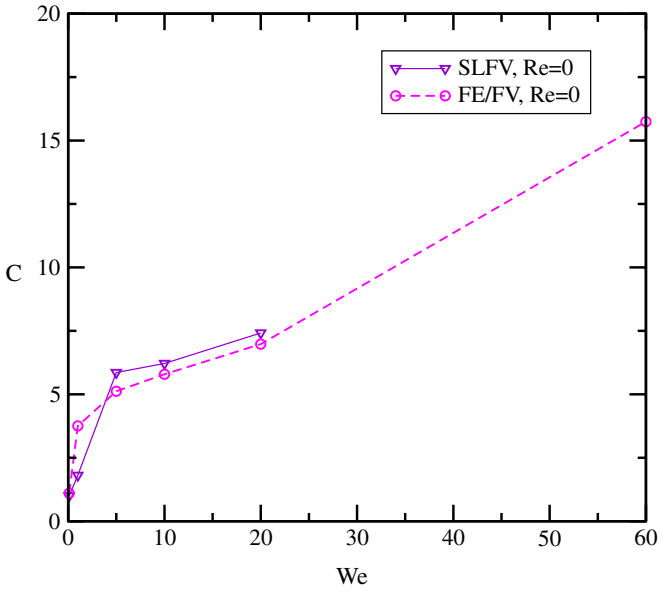

Fig. 23. Couette correction vs. We: SLFV and FE/FV schemes; $Re = 0$.

Finally, Fig. 22 charts total pressure-drop across the domain and its variation with increasing fluid elasticity, for $Re = 0$ and 1. Clearly, both methods predict that pressure-drop is a decreasing function of Weissenberg number below the Newtonian value. This level of inertia is barely significant. In fact, this decline is initially most rapid, falling by some 83% from the Newtonian level to $We = 1$. Then, in proceeding from $We = 1$ to $We = 5$, the pressure drop decreases further by more than 50%. Thereafter, the decline in pressure-drop is more gentle. This can be interpreted through the shear-thinning response of the model, spanning deformation rates between unity and O(10) and noting the moderating influence of increasing We. Again, excellent agreement is observed between results generated with the SLFV and FE/FV schemes. In numerical studies, it is also

common practice to report pressure-drop via the Couette correction (C). This non-dimensional quantity accounts both for the pressure-correction due to the straight channel and the shear properties of the fluid. As such and following Aboubacar et al. [2], we provide in Fig. 23 Couette correction versus We for the creeping flow regime. Here, Couette correction increases monotonically, being due to the shear-thinning properties of the fluid, consistent with the observation of Aboubacar et al. [2] for an EPTT($\epsilon = 0.25$) model. We note that, both SXPP and EPTT($\epsilon = 0.25$) models share similar type of rheological properties both in shear and extension.

5. Conclusions

In this paper, we have contrasted two finite volume schemes and their associated solutions computed over a range of Weissenberg numbers for the XPP model, representing linear-backbone branched polymer melts. Emphasis has been placed upon obtaining viscoelastic solutions in planar, sharp corner contraction geometries. For the hybrid FE/FV scheme, stability and high Weissenberg number solutions have been achieved with a combination of subgrid interpolation for stress, and a consistent treatment of flux and source terms in the momentum equation. This has drawn upon fluctuation distribution and median-dual-cell constructs. Likewise, stability for the pure finite volume schemes (SLFV) has been gathered via a semi-Lagrangian treatment on convection terms, and particularly those within the constitutive equation. Here, second-order area-weighting has been used to evaluate contributions from the previous time-step. Distinction may be drawn between the schemes through their discrete implementation, variable location, control-volume stencils and meshing strategy.

Notwithstanding such differences, excellent agreement has been obtained between these two independent finite volume schemes in the prediction of flow through a 4:1 planar contraction. Quantitative mesh converged data on the size and intensity of the salient-corner vortex have been presented and a detailed mesh convergence study has been performed. Under creeping flow conditions, the cell-size of the vortex has been found to increase with increasing Weissenberg number. Correspondingly, the intensity of the vortex initially has increased with increasing We, before decreasing as the Weissenberg number is increased still further. The presence of inertia has the opposite effect on vortex cell-size, generating decrease with increasing Weissenberg number. Initially, vortex intensity in this case has grown moderately, prior to assuming a steady decline. The XPP model has produced similar trends in vortex behaviour to that for the exponential PTT ($\varepsilon = 0.25$) model. We note, both models share the same type of steady rheological behaviour, being shear-thinning and extension hardening/softening. The dominant feature of larger shear and extension in the entry zone influences stress and stretch, in keeping with the associated rheological properties of the XPP model. Larger stretch develops around the re-entrant corner zone as Weissenberg number increases, whilst correspondingly stress levels decline.

Acknowledgement

The authors acknowledge financial support for the present work from the Engineering and Physical Sciences Research Council, UK under Grants GR/N38619 and GR/N38909.

References

[1] M. Aboubacar, J.P. Aguayo, P.M. Phillips, T.N. Phillips, H.R. Tamaddon-Jahromi, B.A. Snigerev, M.F. Webster, Modelling pom–pom type models with high-order finite volume schemes, J. Non-Newtonian Fluid Mech. 126 (2005) 207–220.
[2] M. Aboubacar, H. Matallah, H.R. Tamaddon-Jahromi, M.F. Webster, Numerical prediction of extensional flows in contraction geometries: hybrid finite volume/element method, J. Non-Newtonian Fluid Mech. 104 (2002) 125–164.
[3] M. Aboubacar, H. Matallah, M.F. Webster, Highly elastic solutions for Oldroyd-B and Phan-Thien/Tanner fluids with a finite volume/element method: planar contraction flows, J. Non-Newtonian Fluid Mech. 103 (2002) 65–103.
[4] M. Aboubacar, T.N. Phillips, H.R. Tamaddon-Jahromi, B.A. Snigerev, M.F. Webster, High-order finite volume methods for viscoelastic flow problems, J. Comput. Phys. 199 (2004) 16–40.
[5] M. Aboubacar, M.F. Webster, A cell-vertex finite volume/element method on triangles for abrupt contraction viscoelastic flows, J. Non-Newtonian Fluid Mech. 98 (2001) 83–106.

[6] J.P. Aguayo, H.R. Tamaddon-Jahromi, M.F. Webster, Extensional response of the pom–pom model through planar contraction flows for branched polymer melts, J. Non-Newtonian Fluid Mech. 134 (2006) 105–126.
[7] M.A. Alves, P.J. Oliveira, F.T. Pinho, On the effect of contraction ratio in viscoelastic flow through abrupt contractions, J. Non-Newtonian Fluid Mech. 122 (2004) 117–130.
[8] M.A. Alves, F.T. Pinho, P.J. Oliveira, Effect of a high-resolution differencing scheme on finite-volume predictions of viscoelastic flows, J. Non-Newtonian Fluid Mech. 93 (2000) 287–314.
[9] G.B. Bishko, O.G. Harlen, T.C.B. McLeish, T.M. Nicholson, Numerical simulation of the transient flow of branched polymer melts through a planar contraction using the 'pom–pom' model, J. Non-Newtonian Fluid Mech. 82 (1999) 255–273.
[10] R.J. Blackwell, T.C.B. McLeish, O.G. Harlen, Molecular drag-strain coupling in branched polymer melts, J. Rheol. 44 (2000) 121–136.
[11] D.V. Boger, Viscoelastic flows through contractions, Annu. Rev. Fluid Mech. 19 (1987) 157–182.
[12] E.O.A. Carew, P. Townsend, M.F. Webster, A Taylor–Petrov–Galerkin algorithm for viscoelastic flow, J. Non-Newtonian Fluid Mech. 50 (1993) 253–287.
[13] E.O.A. Carew, P. Townsend, M.F. Webster, Taylor–Galerkin algorithms for viscoelastic flow: application to a model problem, Numer. Meth. Part. Diff. Eqns. 10 (1994) 171–190.
[14] N. Clemeur, R.P.G. Rutgers, B. Debbaut, On the evaluation of some differential formulations for the pom–pom constitutive model, Rheol. Acta 42 (2003) 217–231.
[15] N. Clemeur, R.P.G. Rutgers, B. Debbaut, Numerical simulation of abrupt contraction flows using double convected pom–pom model, J. Non-Newtonian Fluid Mech. 123 (2004) 105–120.
[16] M. Doi, S.F. Edwards, The Theory of Polymer Dynamics, Oxford University Press, Oxford, 1986.
[17] R.E. Evans, K. Walters, Flow characteristics associated with abrupt changes in geometry in the case of highly elastic liquids, J. Non-Newtonian Fluid Mech. 20 (1986) 11–29.
[18] R.E. Evans, K. Walters, Further remarks on the lip-vortex mechanism of vortex enhancement in planar-contraction flows, J. Non-Newtonian Fluid Mech. 32 (1989) 95–105.
[19] F. Beblida, I.J. Keshtiban, M.F. Webster, Stabilised computations for incompressible and mildly compressible viscoelastic flows, Available as CSR 1-2005, Computer Reports Series, University of Wales, Swansea.
[20] O. Hassager, Working group on numerical techniques, in: Fifth International Workshop on Numerical Methods in Non-Newtonian Flows, Lake Arrowhead, USA, vol. 29, 1988, pp. 2–5.
[21] M.E. Hubbard, P.L. Roe, Multidimensional upwind fluctuation distribution schemes for scalar dependent problems, Int. J. Numer. Meth. Fluids 33 (2000) 711–736.
[22] J.M. Marchal, M.J. Crochet, Hermitian finite elements for calculating viscoelastic flow, J. Non-Newtonian Fluid Mech. 20 (1986) 187–207.
[23] J.M. Marchal, M.J. Crochet, A new mixed finite element for calculating viscoelastic flow, J. Non-Newtonian Fluid Mech. 26 (1987) 77–114.
[24] G. Marrucci, Dynamics of entanglements: a non-linear model consistent with the Cox–Merz rule, J. Non-Newtonian Fluid Mech. 62 (1996) 279–289.
[25] T.C.B. McLeish, R.G. Larson, Molecular constitutive equations for a class of branched polymers: The pom–pom polymer, J. Rheol. 42 (1) (1998) 81–110.
[26] J. Van Meerveld, Note on thermodynamic consistency of the integral pom–pom model, J. Non-Newtonian Fluid Mech. 108 (2002) 291–299.
[27] R.G. Owens, T.N. Phillips, Computational Rheology, Imperial College Press, London, 2002.
[28] S.V. Patankar, Numerical Heat Transfer and Fluid Flow, Hemisphere Publishing, New York, 1981.
[29] T.N. Phillips, A.J. Williams, Viscoelastic flow through a planar contraction using a semi-Lagrangian finite volume method, J. Non-Newtonian Fluid Mech. 87 (1999) 215–246.
[30] T.N. Phillips, A.J. Williams, Conservative semi-Lagrangian finite volume schemes, Numer. Meth. Part. Diff. Eqns. 17 (2001) 403–425.
[31] T.N. Phillips, A.J. Williams, Comparison of creeping and inertial flow of an Oldroyd B fluid through planar and axisymmetric contractions, J. Non-Newtonian Fluid Mech. 108 (2002) 25–47.
[32] B. Purnode, M.J. Crochet, Flows of polymer solutions through contractions. part I: flows of polyacrylamide solutions through planar contractions, J. Non-Newtonian Fluid Mech. 65 (1996) 269–289.
[33] I. Sirakov, A. Ainser, M. Haouche, J. Guillet, Three-dimensional numerical simulation of viscoelastic contraction flows using the pom–pom differential constitutive model, J. Non-Newtonian Fluid Mech. 126 (2005) 163–173.
[34] R.I. Tanner, S. Nasseri, Simple constitutive models for linear and branched polymers, J. Non-Newtonian Fluid Mech. 116 (2003) 1–17.
[35] R.G.M. van Os, T.N. Phillips, The prediction of complex flows of polymer melts using spectral elements, J. Non-Newtonian Fluid Mech. 122 (2004) 287–301.
[36] W.M.H. Verbeeten, G.W.M. Peters, F.T.P. Baaijens, Differential constitutive equations for polymer melts: the eXtended pom–pom model, J. Rheol. 45 (4) (2001) 823–843.
[37] W.M.H. Verbeeten, G.W.M. Peters, F.P.T. Baaijens, Viscoelastic analysis of complex polymer melt flows using the eXtended pom–pom model, J. Non-Newtonian Fluid Mech. 108 (2002) 301–326.
[38] W.M.H. Verbeeten, G.W.M. Peters, F.P.T. Baaijens, Numerical simulations of the planar contraction flow for a polyethylene melt using the XPP model, J. Non-Newtonian Fluid Mech. 117 (2004) 73–84.

[39] K. Walters, M.F. Webster, The distinctive CFD challenges of computational rheology, Int. J. Numer. Meth. Fluids 43 (2003) 577–596.
[40] P. Wapperom, M.F. Webster, Simulation for viscoelastic flow by a finite volume/element method, Comput. Meth. Appl. Mech. Eng. 180 (1999) 281–304.
[41] M.F. Webster, H.R. Tamaddon-Jahromi, M. Aboubacar, Time-dependent algorithms for viscoelastic flow – finite element/volume schemes, Numer. Meth. Part. Diff. Eqns. 121 (2005) 272–296.
[42] M.F. Webster, H. Matallah, K.S. Sujatha, Sub-cell approximation for viscoelastic flows-filament stretching, J. Non-Newtonian Fluid Mech. 126 (2005) 187–205.
[43] S.-C. Xue, N. Phan-Thien, R.I. Tanner, Three dimensional numerical simulations of viscoelastic flows through planar contractions, J. Non-Newtonian Fluid Mech. 74 (1998) 195–245.
[44] J.Y. Yoo, Y. Na, A numerical study of the planar contraction flow of a viscoelastic fluid using the SIMPLER algorithm, J. Non-Newtonian Fluid Mech. 39 (1991) 89–106.